# Clustering of hydrogen, phosphorus, and vacancies in diamond: A density functional theory analysis

Kamil Czelej,* Marcin Roland Zemła, Paulina Kamińska, Piotr Śpiewak, and Krzysztof Jan Kurzydłowski
*Materials Design Division, Faculty of Materials Science and Engineering, Warsaw University of Technology, Wołoska 141, 02-507 Warsaw, Poland*

(Received 26 February 2018; revised manuscript received 23 April 2018; published 29 August 2018)

Phosphorus-doped $n$-type diamond is currently one of the most promising wide-band-gap materials for next-generation high-power electronics and optoelectronics. Artificial diamond growth methods such as chemical vapor deposition involve hydrogen-containing precursors; therefore, the hydrogen atoms can be simultaneously introduced into the diamond lattice as a contamination and form complexes with other defects. In this work, we used the spin-polarized, hybrid density functional theory method to investigate the electronic structure, stability, and magnetic and optical properties of phosphorus, vacancy, and hydrogen clusters in diamond. Our results indicate a thermodynamic driving force for the formation of previously unidentified phosphorus-vacancy-hydrogen complexes that can be electrically, magnetically, or optically active centers. We found an unusual extremely large hyperfine coupling with the $^{31}$P nuclei ($A > 2$ GHz) for some of the investigated defects that requires further experimental verification. Finally, we demonstrate that the $PV_2H^0$ complex has two metastable triplets between the ground- and excited-state singlets, and it may exhibit a highly selective spin decay channel to a ground state, which makes the defect a promising candidate for realizing long-living solid-state quantum memory. These results provide deep insight into the donor compensation effect associated with vacancy-related clusters, and they may be useful in future identification of P-related defects suitable for quantum information processing applications.

DOI: 10.1103/PhysRevB.98.075208

## I. INTRODUCTION

High-quality diamond crystals exhibiting $n$-type conductivity are critical for the development of next-generation high-power electronics and optoelectronics [1–4]. Despite many efforts devoted to fabrication of $n$-type diamond samples by probing a variety of theoretically anticipated shallow dopants [5–17], only the application of phosphorus has led to reasonable $n$-type conductivity. For most $n$-type diamond films doped with P, however, the activation energy of 0.6 eV [18] is rather high, resulting in highly resistive layers with low equilibrium carrier density $n_0 = 10^{10}$ cm$^{-3}$ and electron mobility $\mu_e = 100$ cm$^2$ V s$^{-1}$ at 300 K in the case of $2 \times 10^{18}$ cm$^{-3}$ phosphorus-doped layers [19]. In fact, a higher Hall mobility $\mu_e = 1000$ cm$^2$ V s$^{-1}$ has been reported for low compensated P-doped diamond films [20], but this value is still half the typical electron mobility measured in undoped diamond crystals [21]. Considerable progress in heavy phosphorus doping has enabled a reduction of the activation energy to 0.43 eV at a doping concentration of $2 \times 10^{19}$ cm$^{-3}$, and thus it opened up a new avenue for a significant conductivity improvement of $n$-type diamond [22]. An alternate approach to increasing diamond conductivity is to utilize the hopping conduction [23] that emerges above the phosphorus concentration of $>10^{20}$ cm$^{-3}$. To achieve such a high dopant concentration, however, the solubility of P in diamond must be significantly increased, which poses a formidable challenge based on contemporary techniques for doping artificially grown diamonds.

Another major factor affecting conductivity and magneto-optical properties of P-doped diamond is the coexistence of different point defects and their complexes. Specifically, the vacancy-related defects in diamond are commonly known for being deep acceptors; therefore, they act as strong donor compensation centers [24]. As chemical vapor deposition (CVD) grown diamond usually contains a high concentration of vacancies (up to $5 \times 10^{18}$ cm$^{-3}$) [25], the compensation effect associated with vacancy-related defects may lead to a highly resistive material. An ideal $n$-type diamond should contain a large fraction of substitutional P and at the same time it should be vacancy-free. Thus, a thorough understanding of the formation mechanisms, electronic structure, and thermodynamics of vacancy-related complexes in diamond is undoubtedly crucial to the design of highly efficient doping technology.

Recently, a fingerprint of several P-containing paramagnetic centers was detected in synthetic diamonds grown with phosphorus additions [26,27]. Beside the common MA1 center consisting of one substitutional P with the electron spin $S = \frac{1}{2}$, a family of vacancy- and nitrogen-related complexes NP1-NP6 was found and characterized via electron paramagnetic resonance (EPR) spectroscopy [26,27]. The NP1-NP3 centers have an electron spin $S = \frac{1}{2}$ and the hyperfine structure (HFS) of one phosphorus and one nitrogen atom. The proposed atomic structure of these complexes is a phosphorus-nitrogen substitutional pair separated by two and one carbon atom in the case of NP1 and NP2, and a phosphorus-nitrogen substitutional dimer in the case of NP3. It has been shown that high-temperature annealing at 2600 K leads to the formation of new paramagnetic centers (NP4, NP5, and NP6) and the simultaneous disappearance of NP1, NP2, and NP3 [26,27]. On this basis, one may suggest the transformation of NP1-NP3 into NP4-NP6. The analysis of $^{31}$P HFS indicates relatively low spin density on the P atom, which is typical for so-called

*kamil.czelej@inmat.pw.edu.pl

 

TABLE I. The calculated formation energies in a neutral charge state, defect charge transition levels, and hydrogen binding energy for several H-related complexes in diamond in comparison to substitutional dopants. The Fermi energy level is set to 0 eV with respect to the VBM.

| Defect | Formation energy (eV) | Defect charge transition level (eV) | Binding energy (eV) |
|---|---|---|---|
| $N_s$ | 3.96[a] | (+/0) CBM − 1.80[a] | |
| | 4.00[b] | (+/0) CBM − 1.90[b] | |
| NH | | (+/0) VBM + 1.50[c] | 3.5[c] |
| | 5.19[a] | (+/0) CBM − 4.50[a] | |
| NVH | | (0/−) VBM + 2.40[a] | 5.8[d] |
| | | (−/2−) VBM + 4.40[a] | |
| $P_s$ | 6.65[e] | (+/0) CBM − 0.37[e] | |
| | 4.98[f] | (+/0) CBM − 0.67[f] | |
| PH | 7.20[c] | (+/0) CBM − 3.00[c] | ∼0.0[c] |
| | | | 2.56[h] |
| $S_s$ | 10.67[e] | (+/0) CBM − 0.77[e] | |
| SH | ∼12.50[g] | (+/0) VBM + 3.90[i] | 2.18[h] |
| $SVH_3$ | ∼12.00[g] | (+/0) VBM + 4.36[g] | |
| $B_s$ | 2.00[b] | (0/−) VBM + 0.20[i] | |
| | 1.13[e] | (0/−) VBM + 0.39[b] | |
| BH | | (0/−) VBM + 4.44[j] | 1.6[c] |
| | | (+/0) CBM − 4.84[j] | |

[a]Reference [54].
[b]Reference [44].
[c]Reference [31].
[d]Reference [34].
[e]Reference [32].
[f]Reference [18].
[g]Reference [35].
[h]Reference [36].
[i]Reference [37].
[j]Reference [38].

split-vacancy configurations. Among these three centers, NP5 and NP6 have a split-phosphorus-vacancy structure with one substitutional nitrogen in the second and third coordination spheres, whereas the NP4 center is a high-symmetry split-phosphorus-vacancy (PV) defect. To the best of our knowledge, only the electronic structure of the NP4 defect has been analyzed theoretically using a first-principles cluster method [24]. The authors predicted a high $D_{3d}$ symmetry and lack of internal optical transitions for the most realistic negatively charged state of the defect. On the other hand, the clustering of hydrogen with various point defects in diamond including vacancy [28,29] and nitrogen-vacancy [30], and its interaction with substitutional dopants such as phosphorus [31,32], boron [31], nitrogen [31], and sulfur [32], have been widely investigated by means of theoretical and experimental approaches. The vast majority of theoretical investigations are focused mainly on formation energies and defect charge transition levels. To summarize the most essential theoretical data obtained for several previously reported H-related complexes in diamond with respect to their substitutional counterparts, we provide Table I. Large positive values of H binding energies for any given complex indicate a strong tendency toward the formation of H-related clusters in diamond. Based on these results, one may notice that hydrogen in diamond is very common, and the understanding of its impact on the properties of other defects is of paramount importance. P-doped diamond crystallization from gas phase is carried out under nonequilibrium CVD conditions, where an extremely small amount of carbon source is diluted in hydrogen (typically $[CH_4]/[H_2] = 0.1$–$0.3\%$) [33]. Therefore, the hydrogen atoms can be simultaneously introduced into the diamond lattice as a contaminant and form complexes with other defects. Surprisingly, very little is known about these complexes in diamond. In this paper, we used plane-wave, spin-polarized density functional theory to investigate the complexes of multiple hydrogen atoms with PV and $PV_2$ defects in diamond. We predicted relatively low formation energy for some of these defects and a favorable hydrogen clustering effect. We thoroughly discussed the electronic structure of the complexes by using the elements of group theory and the HSE06 calculated Kohn-Sham eigenvalue spectra. To mediate future identification of the unknown phosphorus-vacancy-hydrogen centers in diamond, we calculated their EPR signals, quasilocal vibrational modes, and optical fingerprints. Our EPR results revealed an extremely large hyperfine coupling with the $^{31}P$ nuclei ($A > 2$ GHz) for some defects that is highly unique and requires an experimental verification. Finally, we demonstrated the optical spin polarization cycle of $PV_2H^0$ complex in diamond that may serve as a basis toward the realization of long-living solid-state quantum memory.

## II. COMPUTATIONAL DETAILS

The electronic structure calculations have been carried out using spin-polarized density functional theory (SP-DFT) with the projector augmented wave (PAW) [39,40] method as implemented in the Vienna Ab initio Simulation Package (VASP). We applied the screened, range-separated, nonlocal hybrid functional HSE06 of Heyd, Ernzerhof, and Scuseria [41,42] with the original parameters of 0.207 $Å^{-1}$ for screening and 25% mixing to calculate the equilibrium geometries, ground-state charge, and spin densities of the system. It has been demonstrated that HSE06 in group-IV semiconductors satisfies the generalized Koopmans' theorem [43]. Due to the error compensation between the Hartree-Fock and GGA exchange, HSE06 in diamond turned out to be nearly free of the electron self-interaction error and is capable of providing defect levels and defect-related electronic transitions within 0.1 eV, with respect to experiment [44]. To minimize finite-size effects, we chose a periodic, cubic supercell of $N = 512$ atoms. Such a large supercell enables the approximation of the first Brillouin zone (BZ) using the Γ-point, at which the degeneracy of Kohn-Sham wave functions can be inspected. Our previous studies showed that this setup reproduces known experimental values accurately in the case of point defects in diamond [44,45] and silicon [46]. Convergence parameters and the equilibrium lattice constant were determined in a bulk calculation on a primitive cell. A Brillouin zone (BZ) sampling with an $8 \times 8 \times 8$ Monkhorst-Pack [47] mesh ($k_{MP} = 8^3$) and a plane-wave cutoff energy of 520 eV assure convergence of the charge and spin densities. As a result, an equilibrium lattice parameter of $a_{HSE} = 3.549$ Å and an indirect band gap of $E_g = 5.32$ eV agree well with the experimental values of $a = 3.567$ Å and $E_g = 5.48$ eV, respectively [48]. Defects in

the supercell were allowed to relax in constant volume until the Hellmann-Feynman forces acting on the atom were smaller than 0.01 eV $Å^{-1}$.

We calculated the formation energies of the defects $\Delta H_f^q$ as a function of the electron chemical potential $E_F$ ($\mu_{e|_{T=0\,K}} = E_F$) in the band gap using the standard approach:

$$\Delta H_f^q = E_{\rm tot}^q - \sum_i n_i \mu_i - q(E_{\rm VBM} - E_F) + \Delta E_{\rm corr}, \quad (1)$$

where the Fermi level $E_F$ is referenced to the valence band maximum (VBM) of perfect diamond, $q$ is the charge state of a defect, $E_{\rm tot}^q$ is the total energy of a defect-containing supercell, and $\mu_i$ stands for the chemical potential of the corresponding atoms ($i$ = C, P, H). The $\mu_C$ value is determined from the total energy of a perfect diamond lattice, whereas $\mu_P$ is deduced from the gas phase $PH_3$. The last term $\Delta E_{\rm corr}$ is the charge correction in total energy due of the defective supercell. After the electrostatic potential alignment, we applied $\frac{2}{3}$ of the monopole term of the Makov-Payne charge correction [48,49] to compute $\Delta E_{\rm corr}$. This correction scheme provides equivalent values with the Freysoldt correction [50,51], and it is capable of reproducing the experimentally measured ionization energy of deep states in group-IV semiconductors [52] including diamond [53,54] within an accuracy of ∼0.1 eV. The adiabatic charge transition levels $E^{q|q+1}$ for a selected point defect can be calculated using the following formula:

$$E^{q|q+1} = \Delta H_f^q - \Delta H_f^{q+1}. \quad (2)$$

To verify the clustering of hydrogen atoms on the complexes investigated, we calculated the binding energy of hydrogen. Here, we assumed the model of mobile interstitial hydrogen ($H_i$) that can be trapped by $PVH_n$ or $PV_2H_n$ and form $PVH_{n+1}$ or $PV_2H_{n+1}$ clusters, respectively. The existence of mobile hydrogen in diamond under the CVD growth condition that we assumed in our paper is indeed necessary to its clustering with vacancy-related complexes. Previous theoretical investigation conducted by Goss *et al.* [31] shows high mobility of H, in particular in a $H^+$ charge state, with a very low activation barrier. Another theoretical work by Herrero *et al.* [55] confirms that finding and provides the temperature dependence of hydrogen jumping rates in bulk diamond. Ultimately, experimental measurements revealed that hydrogen diffusion is already observed at 850 K in defect containing diamonds [56], and hence the assertion of mobile hydrogen is justified. The binding energy can be defined as follows:

$$E_b = \Delta H_f^{q1}(PVH_n) + \Delta H_f^{q2}(H_i) - \Delta H_f^{q3}(PVH_{n+1}) + \sum_j^3 q_j E_F. \quad (3)$$

According to this definition, positive binding energy indicates a tendency toward cluster formation. As can be seen, the binding energy depends on the actual position of the Fermi energy level; therefore, we calculated two values of $E_b$ assuming a significantly larger concentration of single vacancy than substitutional phosphorus and vice versa.

To calculate the potential energy surface (PES) of the excited states and the corresponding ZPL values, we applied the constrained density functional theory ΔSCF method [57] implemented in VASP code. This method allows one to determine the relaxation energy of the atomic cores due to optical excitation. We decided to use the ΔSCF procedure with the HSE06 hybrid functional instead of a fully nonlocal dynamical screened Coulomb interaction approach to calculate the ZPL because it is much less computationally demanding and provided excellent agreement with absorption and photoluminescence experiments for a variety of well-known complexes in diamond, including $NV^{1-}$ [57], SiV [53], $SiV_2H^{1-}$ [58], and $OV^{1+}$ [61].

We used the VASP implementation of density functional perturbation theory (DFPT) to calculate the phonon spectrum of the systems. In this case, we applied the Perdew-Burke-Ernzerhof (PBE) approximation in the Hamiltonian. The selection of PBE for computing the vibrational modes and frequencies is dictated by the following reasons: (i) It has been demonstrated that the PBE approximation is able to accurately reproduce the experimental lattice constant of diamond, the phonon spectrum, as well as their dependence on pressure and temperature [62]. In fact, the calculated Raman mode of 1336 $cm^{-1}$ for the perfect 512 atomic supercell is very close to the experimental value of 1332 $cm^{-1}$ [63]. (ii) The application of a nonlocal hybrid functional in this case is beyond the computational power of our facilities since we allow all atoms to vibrate, and as a result, for lower symmetry defects there are >1000 vibrational degrees of freedom. To calculate the quasilocal vibrational modes with high precision, we applied a very strict $10^{-4}$ eV $Å^{-1}$ force convergence criterion. The normal modes were analyzed using the inverse participation ratio approach [64]. The zero-field splitting (D tensor) due to electron-spin–electron-spin interaction was calculated within the framework recently implemented in the VASP code [65]. We calculated the hyperfine tensor including the core spin polarization effect in the Fermi contact within the frozen valence approximation, using the VASP implementation suggested by Szász *et al.* [66]. In this case, the plane-wave cutoff energy was raised to 800 eV.

## III. RESULTS AND DISCUSSION

Our analysis encompasses the hydrogen clusters with single-vacancy phosphorus: $PVH_n$, where $n = 1, 2, 3$; and bivacancy phosphorus: $PV_2H_n$, where $n = 1, 2, \ldots, 6$ in diamond. To evaluate the tendency toward hydrogen clustering, we first calculated the binding energy of hydrogen atoms to these complexes (see Table II). Such large values of hydrogen binding energies are due to two reasons. First of all, the binding energy of H is calculated with respect to interstitial H in a perfect diamond lattice. Since the interstitial H occupies the central position of the C − C bond, it induces locally a substantial elastic deformation, and as a result, significant strain energy contribution, whereas the H atoms incorporated into the vacancy passivate the dangling bonds without noticeable elastic deformation. Secondly, the nature of the C − H bond in the vacancy is different from the C − H − C bond in the interstitial site. In the case of vacancy, a strong covalent C − H bond with high dissociation

TABLE II. Binding energies of a hydrogen atom to the $PVH_n$ and $PV_2H_n$ complexes calculated for the most stable charge state of the defect at $E_F = 2.29$ and 4.72 eV.

| | $E_b$ (eV) | | | $E_b$ (eV) | |
|---|---|---|---|---|---|
| $E_F =$ | 2.29 | 4.72 | $E_F =$ | 2.29 | 4.72 |
| PVH | 3.57 | 0.74 | $PV_2H$ | 6.51 | 5.44 |
| $PVH_2$ | 3.66 | 3.39 | $PV_2H_2$ | 5.42 | 3.75 |
| $PVH_3$ | 4.86 | 2.01 | $PV_2H_3$ | 5.50 | 3.06 |
| | | | $PV_2H_4$ | 1.67 | 0.80 |
| | | | $PV_2H_5$ | 3.73 | 3.42 |
| | | | $PV_2H_6$ | 4.99 | 2.58 |

energy is formed, whereas in the case of interstitial H, the C − H − C bond is known as three-center electron deficient bonding, for which the dissociation energy is significantly smaller. A combination of these two factors is responsible for very large values of hydrogen binding energies for vacancy-related clusters. In the case of *n*-type diamond, where the vast majority of P atoms occupy the substitutional sites ($P_s$), the Fermi energy pins close to the $1+/0$ charge transition level of the $P_s$ defect, which is found to be at $E_{\mathrm{VBM}}$ 4.72 eV. On the other hand, when the concentration of vacancies in diamond is significantly larger than the concentration of $P_s$, the Fermi energy is located near the $0/1-$ charge transition level of a single vacancy at $E_{\mathrm{VBM}}$ + 2.29 eV. Hence, the most realistic Fermi level position, assuming the coexistence of substitutional phosphorus and vacancy-related complexes in diamond, is located between 2.29 and 4.72 eV with respect to the VBM. The calculated positive binding energy values for both $E_F = E_{\mathrm{VBM}} + 2.29$ eV and $E_F = E_{\mathrm{VBM}} + 4.72$ eV reveal the thermodynamic driving force for complex formation in hydrogen-contaminated diamond.

According to our HSE06 results, all the investigated complexes with hydrogen atoms can theoretically occur within the relevant range of Fermi energy levels. The relaxed geometries of the complexes together with the point-group symmetry labels are depicted in Fig. 1. Next, we calculated the formation energy of these defects as a function of Fermi level position in the fundamental band gap of diamond (see Fig. 2). Based on these charts, one can anticipate the relative stability of a given complex in various charge states with respect to other complexes. It can be seen that the hydrogen atoms push the phosphorus out of an inversion center of PV defects, and as a result, the formation energy of the $PVH_n$ complex increases with increasing number of H. Interestingly, in the case of $PV_2H_n$, we can partially observe the stabilization effect associated with hydrogen incorporation. Upon relaxation, first, second, and third H migrates to the second vacancy and terminates carbon dangling bonds. The formation of $PV_2H_1$,

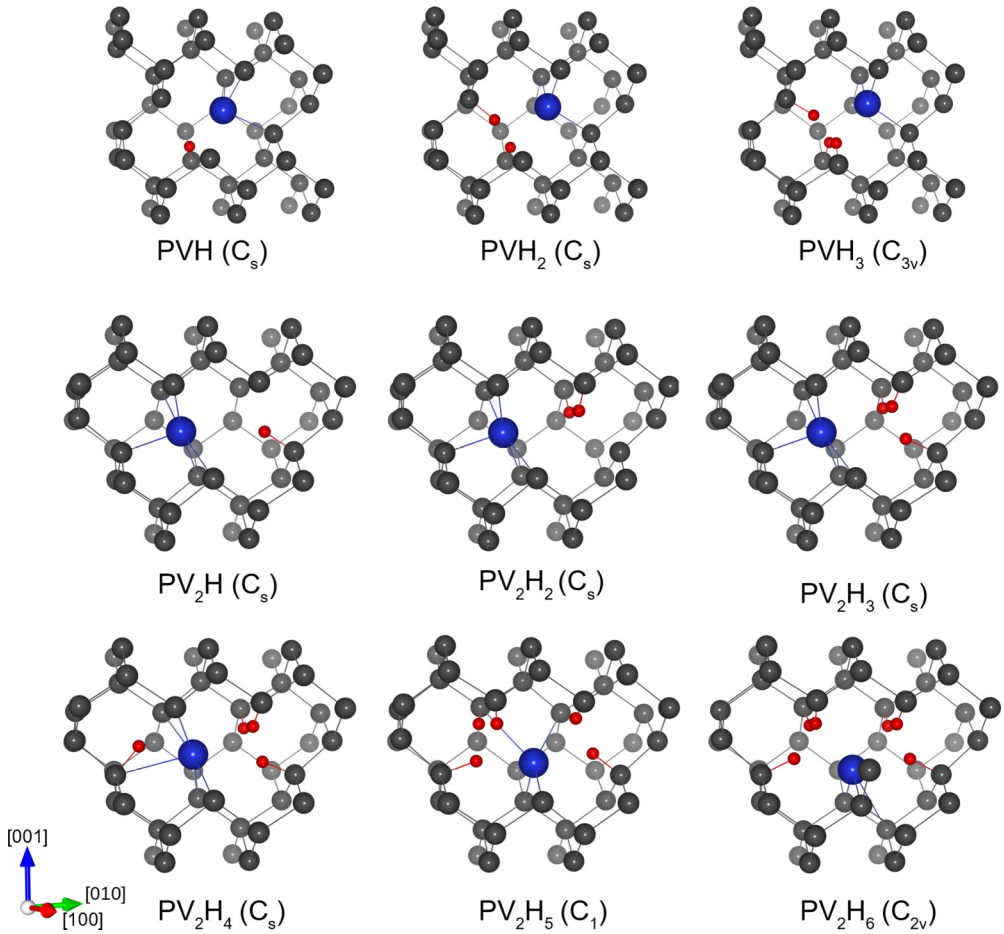


FIG. 1. Ground-state geometries of the investigated complexes extracted from a 512-atom supercell together with the point group symmetry labels. The P atom is represented by a large dark blue ball and the hydrogen atoms by small red balls.

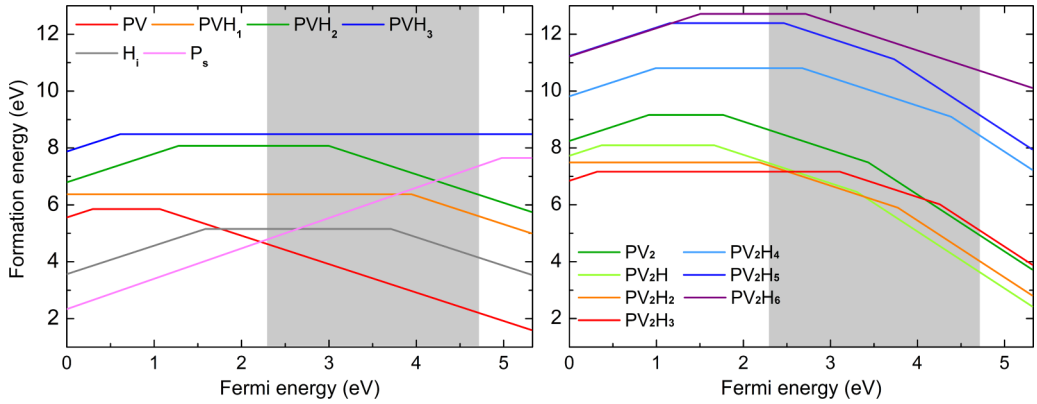


FIG. 2. Formation energy of the investigated complexes as a function of Fermi level position in the fundamental band gap of diamond. The Fermi energy level is referenced to the VBM. The gray shaded area represents the most realistic range of Fermi level positions in P-doped diamond.

$PV_2H_2$, and $PV_2H_3$ is more favorable than $PV_2$ due to their lower formation energy. When more than three hydrogen atoms are considered, the remaining dangling bonds of the second vacancy can be terminated by H, whereas the phosphorus atom is pushed toward the middle of the bivacancy. Figure 2 indicates that the formation energy of $PV_2H_4$, $PV_2H_5$, and $PV_2H_6$ is significantly higher than that of $PV_2$, and therefore their formation probabilities are extremely small. In reality, the formation energies of point defects in diamond are extremely high, and their interpretation based on thermodynamic equilibrium should be made carefully when the existence ratio of different complexes is considered. One has to take into account the fact that growth of artificial diamond is carried out under highly nonequilibrium CVD conditions. The main contribution to the formation energy is the chemical potential of individual components (strongly dependent on the plasma parameters) that builds up the final complex, which in turn depends on the local chemical environment. The local chemical environment obviously changes as a function of time since the complexes are not instantly formed, rather they are created as a result of hydrogen and vacancy migration, and the subsequent clustering effect. As a consequence, complexes of relatively high formation energy calculated from the Arrhenius-like formula based on thermodynamic equilibrium can be found in diamond in a reasonable concentration. The example of such a complex is $SiV_2H$ for which the calculated formation energy is significantly higher than that for simple SiV [58], however $SiV_2H^{1-}$ was experimentally observed and associated with the WAR3 absorber center in diamond.

### A. Single vacancy-related complexes in diamond: $PVH_n$

To understand the electronic structure of $PVH_n$ complexes in diamond it is worthwhile to analyze the ancestor split phosphorus-vacancy defect first. According to our HSE06 results, the defect in its ground state has high $D_{3d}$ symmetry with the inversion center located at P, in accordance with previous studies [24,67]. It can exist in positive, neutral, and negative charge states, whereas the $1+/0$ charge transition level is very close to the VBM and thus is unlikely to occur under typical growth conditions. The calculated acceptor level

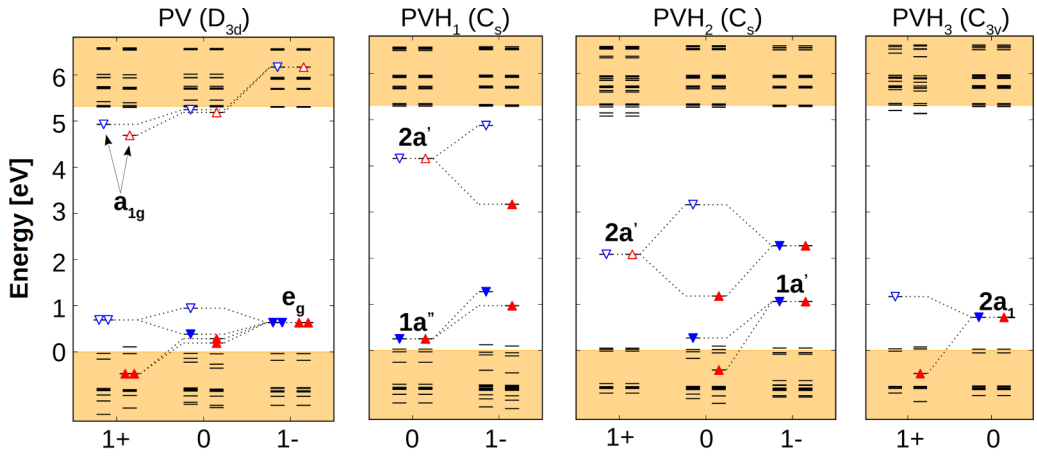


FIG. 3. Localized Kohn-Sham levels of the investigated PV and $PVH_n$ complexes in diamond calculated with the HSE06 hybrid functional. The light orange shaded area represents the conduction and valence band of an ideal diamond. Spin-down (-up) channels are indicated by blue (red) triangles, whereas the filled (unfilled) triangles represent the occupied (empty) states. For the sake of clarity, the corresponding KS states in different charge states are linked by black dotted lines.

TABLE III. Experimental hyperfine structure of several $XVH^q$ complexes, where $X$ = N, Si, O in comparison to $PVH^{1-}$ calculated in our study.

| Defect | Spin state | Nuclei | $A_{xx}$ (MHz) | $A_{yy}$ (MHz) | $A_{zz}$ (MHz) |
|---|---|---|---|---|---|
| $VH^{1-}$ | $S=1$ | $^{1}$H | 1.10(5)[a] | 1.95(5)[a] | 1.95(5)[a] |
| $NVH^{1-}$ | $S=\frac{1}{2}$ | $^{1}$H | $\pm13.7$[b] | $\pm9.0$[b] | $\pm9.0$[b] |
| $SiVH^{0}$ | $S=\frac{1}{2}$ | $^{1}$H | $-7.9$[c] | 4.7[c] | 7.3[c] |
| | | $^{29}$Si | 76[c] | 81[c] | 79[c] |
| $OVH^{0}$ | $S=\frac{1}{2}$ | $^{1}$H | $\mp13.6(1)$[d] | $\pm9.0(1)$[d] | $\pm9.0(1)$[d] |
| $PVH^{1-}$ | $S=\frac{1}{2}$ | $^{1}$H | 55 | 21 | 25 |
| | | $^{31}$P | 3315 | 2971 | 2980 |

[a]Reference [28].
[b]Reference [59].
[c]Reference [60].
[d]Reference [61].

of PV at $E_{\mathrm{VBM}}+1.06$ eV shows excellent agreement with the $E_{\mathrm{VBM}}+1.00$ eV value reported elsewhere [67], being nearly three times shallower than the acceptor level of the single vacancy. Taking into account our consideration concerning the realistic Fermi level position in P-doped diamond, we conclude that only the negatively charged $PV^{1-}$ is likely to be found. The ground state of $PV^{1-}$ is a closed-shell singlet with a fully occupied, doubly degenerate $e_g$ state (see Fig. 3). Since $e_g$ is the only defect state present in the band gap, there are no possible internal optical transitions. In addition, we calculated the vibrational spectrum of the $PV^{1-}$ center that can be captured in infrared absorption or phonon sideband in the photoluminescence experiment. Using the inverse participation ratio analysis (IPR), we identified quasilocal vibrational modes associated with the motion of a P atom at 507 $cm^{-1}$ (doubly degenerate $e_g$ mode with the IPR = 0.07) and 472 $cm^{-1}$ (nondegenerate $a_{1g}$ mode with the IPR = 0.04). Hydrogen termination of one carbon dangling bond in the PV defect leads to the formation of the PVH complex. As a consequence, the symmetry of the defect is lowered to $C_S$. In this crystal field, the doubly degenerate $e_g$ level splits to symmetric $1a'$ and asymmetric $1a''$. Both states $1a'$ and $1a''$ are fully occupied, whereas only $1a''$ appears in the band gap (see Fig. 3). There is one more symmetric defect state lying high in the band gap, which we labeled as $2a'$. To understand the nature of the calculated KS states, we have generated their real-space three-dimensional (3D) contour plots. The KS wave functions are displayed in Fig. 4. As can be seen, the $1a'$ and $1a''$ states are localized entirely on carbon dangling bonds, while the $2a'$ state is localized mostly on phosphorus. The PVH complex is stable in the neutral and negative charge states and possesses a deep acceptor level at $E_{\mathrm{VBM}}+3.95$ eV. The neutral $PVH^0$ has a singlet ground state with two electrons filling the $1a''$ orbital. In the case of negatively charged $PVH^{1-}$, an additional electron occupies the asymmetric $2a'$ state forming a paramagnetic doublet $S=\frac{1}{2}$ spin state that, in principle, can be observed by EPR spectroscopy.

Table III contains a comparison of our results for $PVH^{1-}$ with available experimental EPR data for similar complexes in diamond. Each $XVH^q$ complex reported in the literature reveals very weak hyperfine coupling with $^1$H, which indicates a lack of substantial spin density in close proximity to H. In fact, electronic structure calculations for these defects show spin density localization mainly on C dangling-bond orbitals. Interestingly, we found an extremely large hyperfine coupling with the $^{31}$P nuclei ($A_{xx}=3315$ MHz, $A_{yy}=2971$ MHz, $A_{zz}=2980$ MHz) for $PVH^{1-}$. This result is very unique and requires further discussion; therefore, we address the problem in a separate paragraph. Due to the large separation between $1a''$ and $2a'$, the PVH is not optically active in the visible spectrum range, however an ultraviolet (UV) laser may excite the defect. We also calculated the quasilocal vibrational modes for this complex. Both the C-H stretching and bending modes belong to an $a'$ irreducible representation of the $C_S$ point group. The calculated frequencies and corresponding IPR values for C-H symmetric stretching and bending are 3258 $cm^{-1}$ (0.32) and 1569 $cm^{-1}$ (0.28), respectively. The remaining C-H asymmetric bending mode of $a''$ character is delocalized in a diamond phonon sideband at ~890 $cm^{-1}$. We found three quasilocal vibrational modes associated with P motion: two $a'$ modes at 499 $cm^{-1}$ (0.05) and 453 $cm^{-1}$ (0.02), and one $a''$ mode at 475 $cm^{-1}$ (0.02).

Adding a second hydrogen atom to the PVH complex enables the formation of $PVH_2$. Similar to PVH, the lowest energy configuration of the $PVH_2$ defect has $C_S$ symmetry (see Fig. 1). According to our HSE06 calculations, the defect

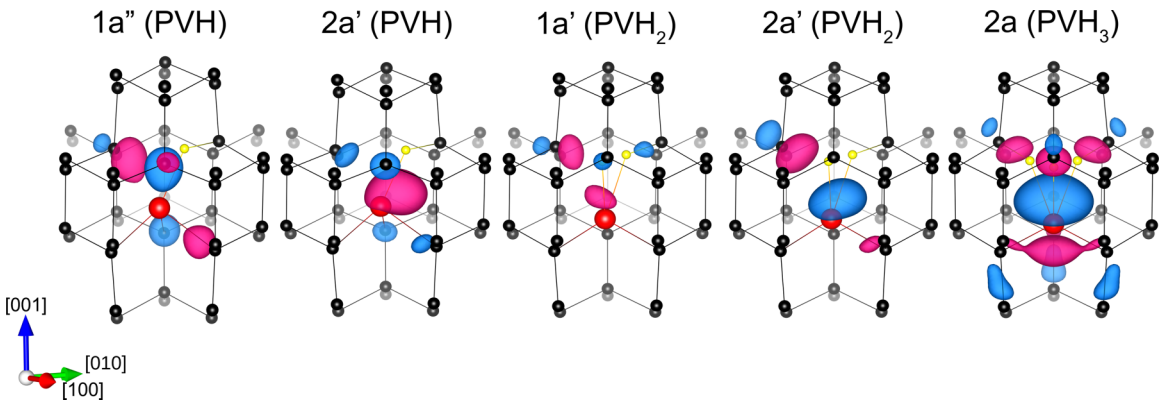


FIG. 4. 3D representation of the calculated Kohn-Sham wave functions for $PVH_n$ complexes in diamond. The red (blue) lobes indicate the positive (negative) phase of the wave functions with an arbitrarily selected isosurface value. Here, the phosphorus, hydrogen, and carbon atoms are represented by red, yellow, and black spheres.

TABLE IV. Hyperfine constants of the $PVH_n$ complexes calculated with the HSE06 functional. The direction of hyperfine constants is provided in spherical coordinates [$R$ (MHz), $\theta$ (deg), $\varphi$ (deg)]. The $\theta$ value describes the polar angle of the [001] direction, whereas $\varphi$ is the azimuthal angle of the [100] direction [on the (100) plane].

| | | $A_{xx}$ | | | $A_{yy}$ | | | $A_{zz}$ | | |
|---|---|---|---|---|---|---|---|---|---|---|
| | No. | $R$ | $\theta$ | $\varphi$ | $R$ | $\theta$ | $\varphi$ | $R$ | $\theta$ | $\varphi$ |
| $PV^0$ | $^{13}$C | 125 | 53° | 225° | 50 | 90° | 135° | 51 | 37° | 45° |
| | $^{31}$P | −227 | 60° | 225° | −187 | 93° | 137° | −182 | 30° | 53° |
| $PVH^{1-}$ | 1 $^{13}$C | 103 | 126° | 308° | 64 | 128° | 183° | 65 | 59° | 245° |
| | 2 $^{13}$C | 103 | 60° | 227° | 64 | 142° | 184° | 65 | 69° | 124° |
| | $^{31}$P | 3315 | 45° | 6° | 2971 | 135° | 0° | 2980 | 87° | 273° |
| | $^{1}$H | 55 | 127° | 222° | 21 | 45° | 180° | 25 | 68° | 294° |
| $PVH_2^0$ | $^{13}$C | 268 | 53° | 130° | 132 | 69° | 23° | 133 | 45° | 27° |
| | $^{31}$P | 1578 | 118° | 212° | 1184 | 58° | 141° | 1234 | 45° | 270° |
| | 1 $^{1}$H | −14 | 57° | 225° | 6 | 108° | 147° | 19 | 39° | 82° |
| | 2 $^{1}$H | −14 | 127° | 138° | 6 | 121° | 21° | 19 | 52° | 83° |

may exist in positive, neutral, and negative charge states, whereas the neutral and negative $PVH_2$ are likely to be found in P-doped diamond. As can be seen in Fig. 3, two localized defect states are present in the band gap: symmetric $1a'$, which originates from the split $e_g$ state of the ancestor PV, and symmetric $2a'$. The remaining asymmetric $1a''$ state falls into the valence band. In the neutral charge state, two electrons occupy the $1a'$ orbital and one electron goes to $2a'$ forming a paramagnetic $S = \frac{1}{2}$ spin state. A significant localization of the $2a'$ wave function on phosphorus (see Fig. 4) leads to large values of hyperfine coupling with the $^{31}$P nuclei ($A_{xx} = 1578$ MHz, $A_{yy} = 1184$ MHz, $A_{zz} = 1234$ MHz). There is only one possible internal optical transition $1a' \rightarrow 2a'$ that may be triggered by near-UV light in the spin minority channel of the neutral $PVH_2$ defect. The negatively charged $PVH_2^{1-}$, however, is optically inactive due to its closed-shell singlet electronic ground state. The defect possesses several distinguishable, quasilocal vibrational modes that may be detected via infrared absorption or the Raman scattering spectrum. We found two high-frequency stretching C-H vibrations at 3489 cm$^{-1}$ (IPR = 0.15; $a'$ character) and 3309 cm$^{-1}$ ($a''$ character; IPR = 0.15), and two $a'$ bending vibrations at 1445 cm$^{-1}$ (IPR = 0.14) and 1340 cm$^{-1}$ (IPR = 0.05). Two remaining bending C-H modes are resonant with the diamond phonon band at 892 and 931 cm$^{-1}$, both with $a''$ character. The low-frequency modes associated with the motion of P are smeared in the phonon sideband at 475 cm$^{-1}$ ($a'$ character), 458 cm$^{-1}$ ($a''$ character), and 354 cm$^{-1}$ ($a'$ character). The calculated hyperfine coupling parameters of the $PVH_n$ are listed in Table IV.

Ultimately, in the case of heavily hydrogenated diamond, a third hydrogen atom can be trapped by $PVH_2$, forming the $PVH_3$ complex. The ground-state configuration of $PVH_3$ has $C_{3v}$ symmetry (see Fig. 1). Theoretically, the defect may exist in positive and neutral charge states, however the stability window of $PVH_3^{1+}$ is very narrow (see Fig. 2); therefore, only the neutral $PVH_3$ may be found in P-doped diamond samples. As shown in Fig. 3, only one, the $2a_1$ state, is present in the band gap. This state is localized on P, H, and C atoms and may be regarded as an antibonding since the wave function changes its sign on H atoms resulting in a different sign on P and the corresponding C atoms (see Fig. 4). The same bonding type has been previously reported for $SiVH_2$ and $SiVH_3$ complexes in diamond [58]. Due to the closed-shell, singlet electronic ground state, the neutral $PVH_3$ is neither optical nor an EPR active center, but it can be detected in infrared absorption experiment. We found two quasilocal stretching C-H modes: one at 3795 cm$^{-1}$ ($a_1$ character; IPR = 0.10) and one doubly degenerate $e$ mode at 3505 cm$^{-1}$ (IPR = 0.15). The calculated high-frequency bending C-H modes are at 1450 cm$^{-1}$ (doubly degenerate $e$; IPR = 0.14) and 1374 cm$^{-1}$ ($a_1$ character; IPR = 0.04). Two remaining bending C-H modes fall into the phonon sideband and lose their quasilocal character. In addition, we report two quasilocal modes associated with a P atom at 332 cm$^{-1}$ ($a_1$ character) and 329 cm$^{-1}$ ($e$ character).

### B. Bivacancy-related complexes in diamond: $PV_2H_n$

High-temperature annealing of P-doped diamond may activate vacancy diffusion and subsequently lead to the formation of $PV_2H_n$ centers. In fact, the PV+V→$PV_2$ reaction is exothermic, and according to our HSE06 calculation it releases 2.9 eV of heat at $E_F = 2.8$ eV. The presence of a second vacancy adjacent to the PV defect provides an additional dangling-bond states in the band gap (see Fig. 5). As a result, the ground-state electronic structure of the $PV_2$ center is complex and depends on its charge state. Our calculations indicate that the defect may exist in positive, neutral, negative, and doubly negative charge states. In a positive charge state, there are three empty states in the band gap: $2a'$, $2a''$, and $3a'$ corresponding to the $C_S$ point group. If one more electron is added to the system, the $2a'$ state originating from the dangling bonds of the second vacancy becomes half-occupied. This, in turn, triggers the so-called pseudo-Jahn-Teller effect, which yields very low $C_1$ symmetry of the entire defect. The same phenomenon has been recently reported for the isoelectronic $SiV_2^{1-}$ complex in diamond [58]. Under the new symmetry, the half-occupied $2a'$ turns into $2a$ and the fully occupied $1a$ (the descendant state of $1a''$) increases clearly above the VB edge (see Fig. 5). The neutral $PV_2$ defect has a paramagnetic $S = \frac{1}{2}$ spin state.

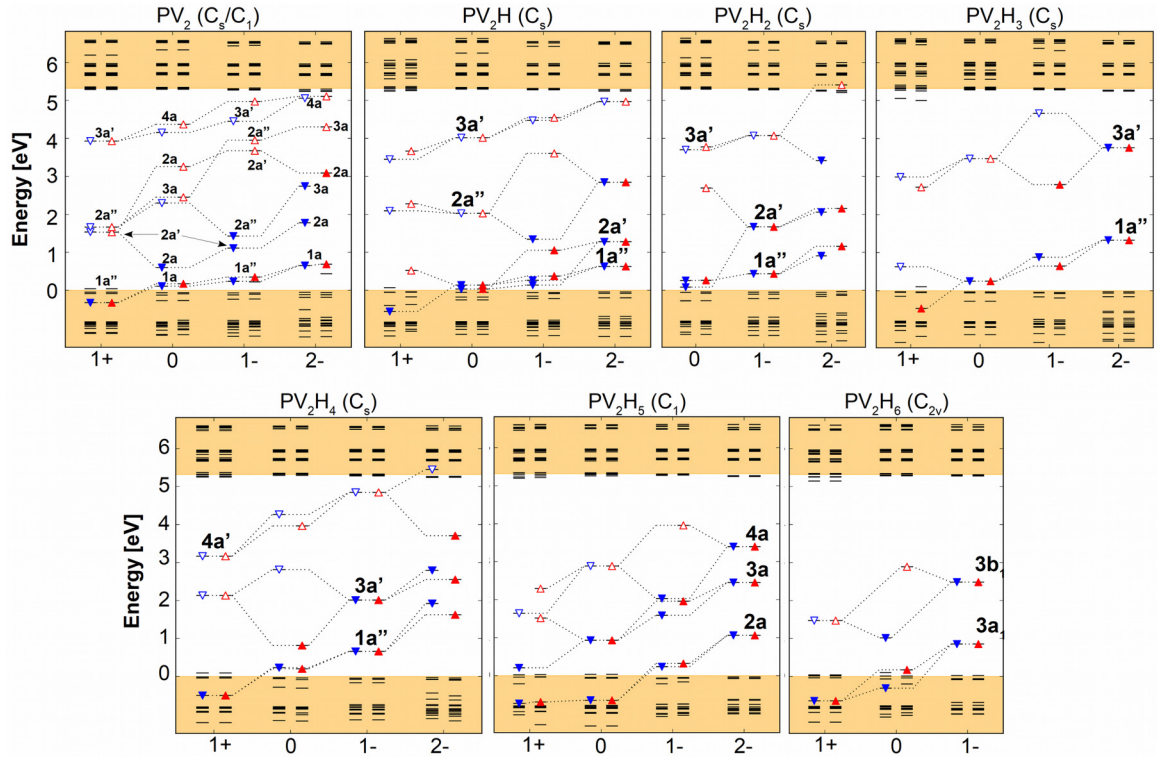


FIG. 5. Localized Kohn-Sham levels of the investigated $PV_2$ and $PV_2H_n$ complexes in diamond calculated with the HSE06 hybrid functional. The light orange shaded area represents the conduction and valence band of an ideal diamond. Spin-down (-up) channels are indicated by blue (red) triangles, whereas the filled (unfilled) triangles represent the occupied (empty) states. For the sake of clarity, the corresponding KS states in different charge states are linked by black dotted lines.

When the next additional electron is considered, the complex is stabilized in $C_S$ symmetry. Interestingly, we found a significant spin polarization of the $PV_2^{1-}$ defect that yields a triplet $S = 1$ spin state with both the $2a'$ and $2a''$ states being half-occupied. Ultimately, the $PV_2$ complex can be ionized to a doubly negative charge state, and again the symmetry is lowered to $C_1$. We found the $PV_2^{2-}$ defect interesting as it possesses the $2a \rightarrow 3a$ internal optical transition in the spin minority channel, which can be triggered by short-wavelength infrared light. The calculated vertical excitation and zero-phonon line values corresponding to the $2a \rightarrow 3a$ optical transition are 0.60 and 0.44 eV, respectively, resulting in 0.16 eV relaxation energy upon optical excitation. By trapping one mobile interstitial hydrogen, the $PV_2$ turns into $PV_2H$. Our HSE06 calculations indicate that the most stable configuration has $C_S$ symmetry with the hydrogen atom lying in the mirror plane of the defect. Multiple localized states can be found in the band gap, as shown in Fig. 5. To corroborate the calculated electronic structure and the group theoretical predictions, we have generated the real-space KS wave functions showing the localization of every individual defect state in the band gap (see Fig. 6). Theoretically, the defect can be stabilized in positive, neutral, negative, and doubly negative charge states (see Fig. 2), whereas $PV_2H^{1+}$ is unlikely to be present in the P-doped diamond. In the neutral charge state, $2a'$ and $1a''$ appear very close to each other just above the VBM and they are fully occupied, resulting in the EPR inactive singlet spin state. In principle, the electron from the $2a'$ and $1a''$ levels can be promoted to the higher level. We calculated the ZPL value for the $2a' \rightarrow 2a''$ optical transition, which is found to be 1.59 eV. In the negative charge state, the additional electron goes to the $2a''$ orbital and builds up a paramagnetic $S = \frac{1}{2}$ spin state that can be observed by EPR. The calculated hyperfine coupling parameters of $PV_2H^{1-}$ are listed in Table V. Finally, the defect may be ionized further to $PV_2H^{2-}$ by adding the second electron to the $2a''$ state, resulting in a nonparamagnetic singlet spin state. We also calculated quasilocal vibrational modes of the $PV_2H$ defect in the negative charge state. The high-frequency stretching and bending vibrations of the C-H segment are at 3021 $cm^{-1}$ ($a'$ character; IPR = 0.29) and 1389 $cm^{-1}$ ($a'$ character; IPR = 0.27), respectively. The second $a''$ C-H bending mode is hybridized with the phonon sideband. We found three low-frequency quasilocal vibrations associated with a P atom at 475 $cm^{-1}$ ($a'$ character), 467 $cm^{-1}$ ($a''$ character), and 399 $cm^{-1}$ ($a'$ character).

Based on the formation energy diagrams, one may conclude that the $PV_2$ complex can easily trap a second and third hydrogen atom and saturate all three dangling bonds of the second vacancy. As a result, the $PV_2H_2$ and $PV_2H_3$ centers may be formed, both having $C_S$ ground-state symmetry. According to our calculations, the former may exist in neutral, negative, and doubly negative charge states, while the latter, in addition, has a narrow stability window in the positive charge state. Nevertheless, the existence of $PV_2H_3^{1+}$ is highly unrealistic in the P-doped diamond samples. In the case of $PV_2H_2$ there are three localized states in the band gap: $1a''$, $2a'$, and $3a'$ (see Fig. 5). As can be seen in Fig. 6, the symmetric $3a'$ state is localized mainly on phosphorus, while $1a''$ and $2a'$ are purely

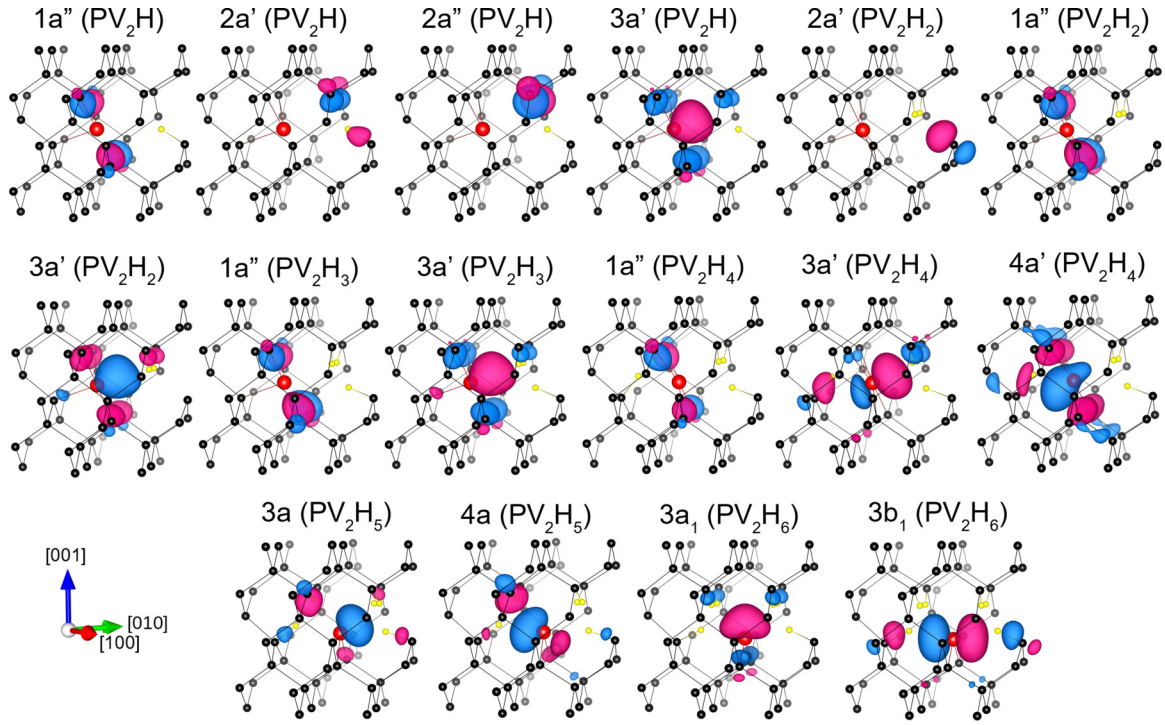


FIG. 6. 3D representation of the calculated Kohn-Sham wave functions for $PV_2H_n$ complexes in diamond. The red (blue) lobes indicate the positive (negative) phase of the wave functions with an arbitrarily selected isosurface value. Here, the phosphorus, hydrogen, and carbon atoms are represented by red, yellow, and black spheres.

TABLE V. Hyperfine constants of the $PV_2H_n$ complexes calculated with the HSE06 functional. The direction of hyperfine constants is provided in spherical coordinates [$R$ (MHz), $\theta$ (deg), $\varphi$ (deg)]. The $\theta$ value describes the polar angle of the [001] direction, whereas $\varphi$ is the azimuthal angle of the [100] direction [on the (100) plane].

| | | $A_{xx}$ | | | $A_{yy}$ | | | $A_{zz}$ | | |
|---|---|---|---|---|---|---|---|---|---|---|
| | No. | $R$ | $\theta$ | $\varphi$ | $R$ | $\theta$ | $\varphi$ | $R$ | $\theta$ | $\varphi$ |
| $PV_2^0$ | 1 $^{13}$C | 349 | 126° | 225° | 150 | 70° | 150° | 150 | 43° | 263° |
| | 2 $^{13}$C | −159 | 124° | 316° | −59 | 131° | 190° | −60 | 59° | 250° |
| | 3 $^{13}$C | 263 | 56° | 315° | 116 | 93° | 227° | 115 | 35° | 140° |
| | $^{31}$P | 58 | 47° | 117° | 73 | 94° | 31° | 67 | 44° | 306° |
| $PV_2^{1-}$ | 1 $^{13}$C | 179 | 124° | 314° | 100 | 79° | 232° | 100 | 36° | 337° |
| | 2 $^{13}$C | 179 | 124° | 136° | 100 | 101° | 38° | 100 | 36° | 113° |
| | 3 $^{13}$C | 200 | 126° | 45° | 103 | 90° | 315° | 102 | 36° | 45° |
| | $^{31}$P | 49 | 88° | 225° | 46 | 90° | 135° | 44 | 3° | 41° |
| $PV_2^{2-}$ | 1 $^{13}$C | 385 | 124° | 317° | 222 | 113° | 211° | 223 | 42° | 274° |
| | 2 $^{13}$C | 355 | 124° | 133° | 210 | 76° | 52° | 210 | 37° | 161° |
| | $^{31}$P | −911 | 67° | 225° | −789 | 99° | 139° | −784 | 25° | 69° |
| $PV_2H_2^{2-}$ | 1 $^{13}$C | 101 | 51° | 311° | 68 | 99° | 228° | 70 | 41° | 149° |
| | 2 $^{13}$C | 101 | 51° | 139° | 68 | 81° | 42° | 70 | 41° | 301° |
| | $^{31}$P | 2587 | 112° | 225° | 2217 | 90° | 135° | 2206 | 22° | 225° |
| | 1 $^{1}$H | 17 | 67° | 78° | −12 | 132° | 11° | −18 | 51° | 327° |
| | 2 $^{1}$H | 17 | 67° | 12° | −18 | 129° | 303° | −12 | 48° | 260° |
| $PV_2H_3^{1-}$ | 1 $^{13}$C | 100 | 130° | 132° | 67 | 80° | 51° | 68 | 42° | 152° |
| | 2 $^{13}$C | 100 | 130° | 318° | 67 | 100° | 219° | 68 | 42° | 298° |
| | $^{31}$P | 1878 | 70° | 45° | 1543 | 90° | 315° | 1537 | 20° | 225° |
| | 1 $^{1}$H | 17 | 117° | 263° | −43 | 60° | 190° | −46 | 43° | 320° |
| | 2 $^{1}$H | 17 | 63° | 7° | −46 | 137° | 311° | −43 | 60° | 260° |
| | 3 $^{1}$H | 21 | 103° | 45° | −1 | 90° | 315° | 0 | 13° | 45° |

dangling-bond states. We found the EPR active, paramagnetic $S = \frac{1}{2}$ spin-state configuration for the neutral and doubly negative charge states. The calculated EPR signals, however, are distinctively different (see Table V) due to a substantial difference in the spin density localization. The negatively charged $PV_2H_2$ complex is found to have a nonparamagnetic singlet spin state and possible internal optical transition within the visible spectrum range. We report the calculated value of the ZPL for the $2a' \rightarrow 3a'$ optical transition to be 1.65 eV. In the case of $PV_2H_3$, only two localized states appear in the band gap: $1a''$ and $3a'$. Both $PV_2H_3^0$ and $PV_2H_3^{2-}$ have a nonparamagnetic singlet spin state, and hence they cannot be captured via EPR spectroscopy. By contrast, $PV_2H_3^{1-}$ has one unpaired electron on the $3a'$ orbital that builds up a paramagnetic doublet spin state. Again, a substantial localization of the $3a'$ wave function on phosphorus yields very large hyperfine coupling with the $^{31}$P nuclei (see Table V). As one may expect, both the $PV_2H_2$ and $PV_2H_3$ centers are rich in quasilocal vibrational modes. The most localized vibrations are those associated with hydrogen. Taking into consideration the negative charge state, we can distinguish two C-H stretching modes at 2892 cm$^{-1}$ ($a'$) and 2545 cm$^{-1}$ ($a''$) for $PV_2H_2^{1-}$, and three C-H stretching modes at 3540 cm$^{-1}$ ($a'$), 3373 cm$^{-1}$ ($a'$), and 3297 cm$^{-1}$ ($a''$) for $PV_2H_3^{1-}$. We also found the C-H bending modes at 1638 cm$^{-1}$ ($a'$), 1344 cm$^{-1}$ ($a''$), and 1335 cm$^{-1}$ ($a'$) for $PV_2H_2^{1-}$, and the C-H bending modes at 1473 cm$^{-1}$ ($a'$), 1469 cm$^{-1}$ ($a''$), and 1432 cm$^{-1}$ ($a'$) for $PV_2H_3^{1-}$. The remaining C-H bending as well as the quasilocal P-related modes fall into the phonon sideband and lose some of their quasilocal character.

As we have already mentioned, the complexes of $PV_2$ with four, five, and six hydrogen atoms seem unrealistic due to their high formation energies, but they cannot be entirely excluded in heavily hydrogenated diamond samples based on their positive H binding energies. Here, we only briefly discuss their electronic structure. In the case of $PV_2H_4$, the fourth hydrogen atom goes to the first vacancy and pushes the P atom slightly toward the middle of the defect. The ground state has $C_S$ symmetry and the defect may be stabilized in 1+, 0, 1−, and 2− charge states. As can be seen in Fig. 6, a new symmetric $4a'$ antibonding state localized on P and the nearest C dangling bonds appears in the band gap. The neutral and doubly negative $PV_2H_4$ can be principally observed via EPR spectroscopy due to their paramagnetic $S = \frac{1}{2}$ spin state. $PV_2H_5$ in turn has very low $C_1$ symmetry. Our calculations show that it can exist in 1+, 0, 1−, and 2− charge states, whereas the 1+ and 1− are paramagnetic $S = \frac{1}{2}$ centers. Ultimately, the sixth hydrogen atom can terminate the remaining dangling bond, leading to the formation of $PV_2H_6$. The defect has higher $C_{2v}$ symmetry and can exist in 1+, 0, and 1− charge states. Following the character table of the $C_{2v}$ point group, we can label two antibonding states in the band gap as symmetric $3a_1$ and asymmetric $3b_1$, both localized mostly on a P atom (see Fig. 6). In the neutral charge state, one electron occupies the $3b_1$ orbital forming a paramagnetic $S = \frac{1}{2}$ spin state.

### C. The origin of extremely large hyperfine coupling with $^{31}$P nuclei

Apart from the identification of point defects in solids, the hyperfine interaction is responsible for quantum entanglement between the electronic and nuclear spin, and therefore it can serve as a basis to realize solid-state quantum bits [68–71]. Recently, Szasz *et al.* [66] implemented an evaluation of a hyperfine tensor into the VASP code. They demonstrated that the combination of a sufficiently large supercell, the HSE06 functional, and the contribution of the core spin polarization to the Fermi contact allows one to accurately reproduce the experimentally measured hyperfine structure in various point defects in semiconductors. We used the same implementation to determine the hyperfine signals for the investigated complexes. Our results of hyperfine coupling tensors are listed in Tables IV and V. We found an extremely large hyperfine coupling with the $^{31}$P nuclei ($A > 2$ GHz) for some of the investigated complexes.

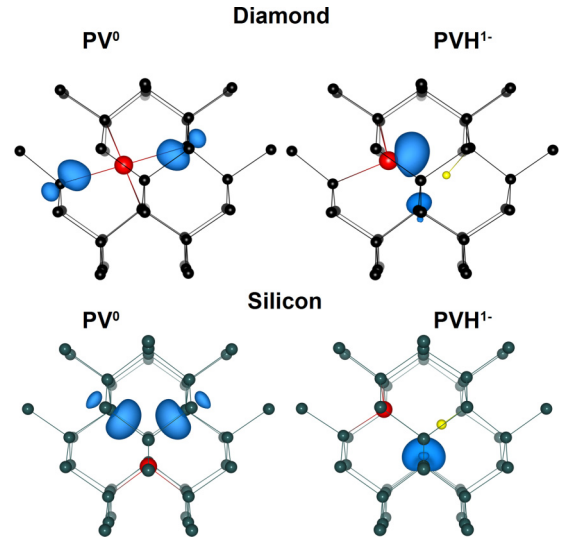


FIG. 7. The calculated spin density isosurfaces of the $PV^0$ and $PVH^{1-}$ complexes in diamond and silicon. The isosurface value is 0.015 and 0.005 for diamond and silicon, respectively. Black, red, and yellow spheres represent the carbon, phosphorus, and hydrogen atoms, respectively.

To the best of our knowledge, these are the highest values of hyperfine constants reported in the literature for solid-state point defects, and they may be a unique feature of the selected P-related complexes in diamond. The large coupling appears when the unpaired electron occupies a strongly localized orbital associated with phosphorus (see Figs. 4 and 6). This in turn leads to nearly entire spin density localization on the P atom, and hence significantly larger coupling with the $^{31}$P nucleus. Otherwise, when the spin electron occupies one of the dangling-bond states, only the indirect spin polarization of the $^{31}$P nuclei takes place, and as a result the calculated hyperfine constants are lower by one order of magnitude. To demonstrate the substantial difference in spin density localization leading to very different hyperfine coupling with $^{31}$P, we visualized the spin density isosurfaces for two selected defects: $PV^0$ and $PVH^{1-}$, keeping the same isosurface value (see Fig. 7). As can be seen, the former complex reveals 100% spin density localization on two C dangling bonds, yielding $A \sim 200$ MHz, whereas the latter shows nearly entire spin density localization on phosphorus, resulting in $A \sim 3000$ MHz. To further clarify the unusual hyperfine coupling with $^{31}$P nuclei in diamond, we calculated the hyperfine tensor and spin density isosurfaces for

analogous complexes in silicon (see Fig. 7). As in the case of diamond, the spin density of $PV^0$ in silicon is localized entirely on dangling-bond orbitals, and the calculated hyperfine constants $^{31}$P: $A_\parallel = 16$ MHz, $A_\perp = 10$ MHz and $^{29}$Si: $A_\parallel = 460$ MHz, $A_\perp = 329$ MHz are in excellent agreement with the available experimental values of $^{31}$P: $A_\parallel = 32$ MHz, $A_\perp = 26$ MHz and $^{29}$Si: $A_\parallel = 450$ MHz, $A_\perp = 295$ MHz [72]. Although $PVH^{1-}$ has the same symmetry in diamond and silicon, the electronic structure and as a result the spin density localization differ significantly for both cases (see Fig. 7). In the case of $PVH^{1-}$ in silicon we observe 100% spin density localization on Si dangling-bond states resulting in small hyperfine coupling with $^{31}$P: $A_\parallel = 11$ MHz, $A_\perp = 10$ MHz. This observation indicates that unusual spin density localization on phosphorus may be a unique feature of certain P- and H-related complexes in diamond, but it still does not explain such large values of hyperfine constants. In general, the hyperfine tensor can be expressed as a sum of an isotropic (Fermi contact) term and an anisotropic (dipolar) term,

$$\left(A^I_{\rm iso}\right)_{ij} = \frac{2}{3}\frac{\mu_0\gamma_e\gamma_I}{\langle S_z\rangle}\delta_{ij}\int \delta_T(\mathbf{r})\rho_s(\mathbf{r}+\mathbf{R}_I)d\mathbf{r}, \quad (4)$$

$$\left(A^I_{\rm ani}\right)_{ij} = \frac{\mu_0\gamma_e\gamma_I}{4\pi\langle S_z\rangle}\int \frac{\rho_s(\mathbf{r}+\mathbf{R}_I)}{r^3}\frac{3r_ir_j-\delta_{ij}r^2}{r^2}d\mathbf{r}, \quad (5)$$

where $\rho_s$ is the spin density, $\mu_0$ is the magnetic susceptibility of free space, $\gamma_e$ is the electron gyromagnetic ratio, $\gamma_I$ is the nuclear gyromagnetic ratio of the nucleus at $\mathbf{R}_I$, and $\langle S_z\rangle$ is the expectation value of the $z$ component of the total electronic spin. $\delta_T$ is a smeared-out delta function. Our calculations for P-V-H complexes in diamond indicate that both contributions are relevant, with the anisotropic term reaching up to ~30% in some cases. As can be seen in Eqs. (4) and (5), the value of hyperfine interaction is highly sensitive to the distance between the localized spin density and the nuclei, and it is proportional to the nuclear gyromagnetic ratio. Due to very high localization of P-related wave functions in the band gap, the electron spin density distribution is highly confined. In fact, we checked by inspection the amplitude of spin density isosurfaces for several P-V-H complexes in diamond. It turned out that if an unpaired electron occupies the P-related orbital, the amplitude is roughly three to five times larger than in the case of C-related dangling bonds. The nuclear gyromagnetic ratio in turn is roughly twice as large for $^{31}$P than $^{13}$C or $^{29}$Si. We conclude that the combination of high spin density within the highly confined P-related orbital and the relatively high gyromagnetic ratio of $^{31}$P are responsible for an extremely large hyperfine coupling for some of the investigated complexes in diamond.

### D. The proposed optical spin polarization cycle of $PV_2H^0$

Recently, Thiering *et al.* [58] have proven that the experimentally observed WAR3 EPR center is associated with the $SiV_2H^{1-}$ complex and its electron spin can be coherently manipulated by optical excitation. Among the considered P-V-H complexes in diamond, the $PV_2H^0$ is isoelectronic and has the same symmetry as the $SiV_2H^{1-}$ center; therefore, it is intriguing to verify whether the $PV_2H^0$ can act as $SiV_2H^{1-}$. Here we demonstrate that an analog optical spin polarization cycle exists and the $PV_2H^0$ might be another interesting candidate for realizing long-living solid-state quantum memory. Upon photoexcitation of the defect with energy close to the ZPL value, the emission of a photon between two singlet $^1A'$ states at ~1.61 eV may occur. We found two metastable triplet $^3A'$ and $^3A''$ shelving states (see Fig. 8) located in between the ground- and excited-state singlets. Low symmetry of the defect leads to the energy splitting of the spin levels due to electron-spin–electron-spin interaction in the absence of an

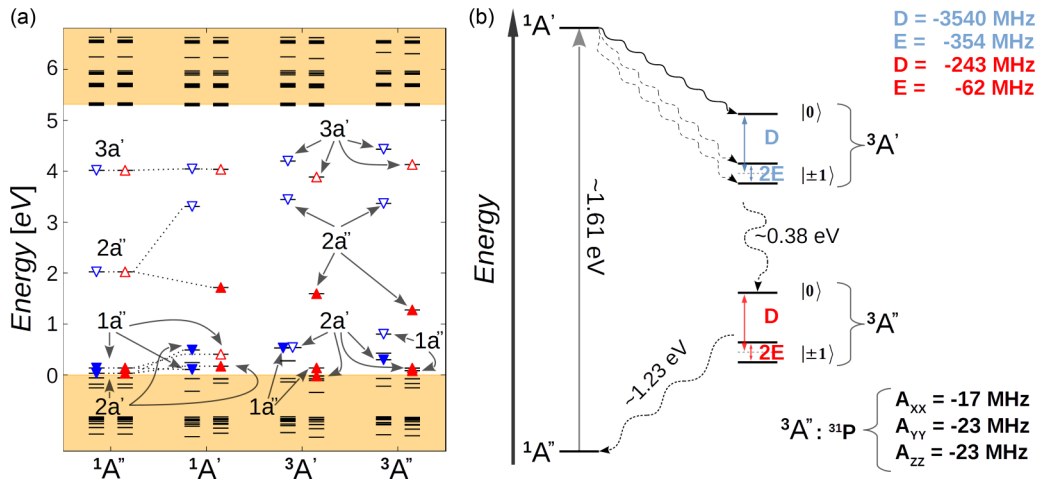


FIG. 8. (a) The HSE06 calculated electronic structure of the ground- and excited-state singlets $^1A'$ and metastable triplets $^3A'$ and $^3A''$. The light orange shaded area represents the conduction and valence band of an ideal diamond. Spin-down (-up) channels are indicated by blue (red) triangles, whereas the filled (unfilled) triangles represent the occupied (empty) states. (b) The Jabłoński diagram describing the proposed spin polarization cycle of the $PV_2H^0$ defect in diamond. Promotion of an electron from $1a''$ to $2a''$ by means of ΔSCF leads to the excited-state singlet $^1A'$. The SOC-mediated ISC gives rise to short-living high-spin electron configuration $^3A'$. The second metastable triplet state $^3A''$ has lower energy. The electron can decay between these two triplets either radiatively or nonradiatively but spin-conserving. Ultimately, the SOC-mediated nonradiative decay from the metastable $^3A''$ to the $^1A'$ ground state closes the optical polarization loop. The zero-field splitting parameters $D$ and $E$ are depicted for both triplets but not scaled for the sake of clarity. The solid thick wavy arrow represents strong while the dotted wavy arrows represent weak SOC-mediated nonradiative decay between the excited $^1A'$ and the metastable $^3A'$ states.

external magnetic field. Spin-orbit coupling (SOC) mediated intersystem crossing (ISC) between the excited state $^1A'$ and the $m_s = 0$ and $\pm 1$ spin sublevels of the metastable $^3A'$ is allowed in the first order. Taking into account different ISC rates between the excited state $^1A'$ and the $m_s = 0$ and $\pm 1$ spin states of the shelving, short-living $^3A'$, it is possible to optically populate the $m_s = 0$ of the metastable $^3A''$. As indicated by Thiering *et al.* [58] for the $SiV_2H^{1-}$ center, the different spin-orbit coupling mediated ISC rates should occur because SOC links the same type of orbitals without changing their character during the ISC process, which is more likely with the $l_z s_z$ operator rather than with $l_+ s_-$ or $l_- s_+$ (the latter would change the character of the orbital). Finally, we calculated the hyperfine coupling with the $^{31}$P nuclei for the metastable triplet $^3A''$ (see Fig. 8). We conclude that quantum information in the metastable $^3A''$ state can be stored by the $^{31}$P nuclear spin mediated by hyperfine coupling, in the same manner as the WAR3 [58] and ST1 [73] centers in diamond.

## IV. SUMMARY AND CONCLUSIONS

Using the spin-polarized, hybrid density functional theory method, we systematically investigated the phosphorus, vacancy, and hydrogen clusters in diamond. Assuming the presence of mobile interstitial hydrogen, we demonstrated a thermodynamic driving force toward the formation of multiple previously unidentified phosphorus-vacancy-hydrogen complexes. To mediate the experimental identification, we calculated their hyperfine structure, quasilocal vibrational modes, and optical signatures. Most of the investigated defects reveal the electrical activity, whereas only two—the $PV_2H$ and $PV_2H_2$—are optically active centers in the visible spectrum range. We found an extremely large hyperfine coupling with the $^{31}$P nuclei ($A > 2$ GHz) for some of the investigated complexes that is very unique and requires further experimental verification. We demonstrated the optical spin polarization cycle of the $PV_2H^0$ complex in diamond that may serve as a basis toward the realization of long-living solid-state quantum memory. Our results should contribute to a better understanding of the electrical activity of P-doped diamond and may be useful in future identification of P-related defects suitable for quantum information processing applications.

## ACKNOWLEDGMENTS

This research was financially supported by the Polish National Science Centre under Contract No. 2012/05/E/ST8/03104. Computing resources were provided by High Performance Computing facilities of the Interdisciplinary Centre for Mathematical and Computational Modeling (ICM) of the University of Warsaw under Grant No. GB69-32. Special acknowledgement goes to Gergő Thiering for helpful suggestions concerning the group theory and the visualization of KS orbitals.

[1] D. Takeuchi, T. Makino, H. Kato, M. Ogura, H. Okushi, H. Ohashi, and S. Yamasaki, Jpn. J. Appl. Phys. **51**, 090113 (2012).
[2] M. Kasu, K. Ueda, Y. Yamauchi, A. Tallaire, and T. Makimoto, Diamond Relat. Mater. **16**, 1010 (2007).
[3] S. Koizumi and M. Suzuki, Phys. Status Solidi A **203**, 3358 (2006).
[4] S. Koizumi, K. Watanabe, M. Hasegawa, and H. Kanda, Science **292**, 1899 (2001).
[5] S. J. Sque, R. Jones, J. P. Goss, and P. R. Briddon, Phys. Rev. Lett. **92**, 017402 (2004).
[6] J. E. Lowther, Phys. Rev. B **67**, 115206 (2003).
[7] S. A. Kajihara, A. Antonelli, J. Bernholc, and R. Car, Phys. Rev. Lett. **66**, 2010 (1991).
[8] R. Li, X. Hu, H. Shen, and X. He, Mater. Lett. **58**, 1835 (2004).
[9] A. B. Anderson and S. P. Mehandru, Phys. Rev. B **48**, 4423 (1993).
[10] M. E. Zvanut, W. E. Carlos, J. A. Freitas Jr., K. D. Jamison, and R. P. Hellmer, Appl. Phys. Lett. **65**, 2287 (1994).
[11] E. Rohrer, C. F. O. Graeff, R. Janssen, C. E. Nebel, M. Stutzmann, H. Güttler, and R. Zachai, Phys. Rev. B **54**, 7874 (1996).
[12] R. Kalish, A. Reznik, C. Uzan-Saguy, and C. Cytermann, Appl. Phys. Lett. **76**, 757 (2000).
[13] J. F. Prins, Phys. Rev. B **61**, 7191 (2000).
[14] E. Lombardi and A. Mainwood, Diamond Relat. Mater. **17**, 1349 (2008).
[15] U. Schwingenschlögl, A. Chroneos, C. Schuster, and R. W. Grimes, J. Appl. Phys. **110**, 056107 (2011).
[16] Q. Y. Shao, G. W. Wang, J. Zhang, and K. G. Zhu, Condens. Matter Phys. **16**, 13702 (2013).
[17] J. E. Moussa, N. Marom, N. Sai, and J. R. Chelikowsky, Phys. Rev. Lett. **108**, 226404 (2012).
[18] K. Czelej, P. Śpiewak, and K. J. Kurzydłowski, MRS Adv. **1**, 1093 (2016).
[19] P. Ščajev, J. Jurkevičius, J. Mickevičius, K. Jarašiūnas, and H. Kato, Diamond Relat. Mater. **57**, 9 (2015).
[20] J. Pernot, C. Tavares, E. Gheeraert, E. Bustarret, M. Katagiri, and S. Koizumi, Appl. Phys. Lett. **89**, 122111 (2006).
[21] M. Nesladek, A. Bogdan, W. Deferme, N. Tranchant, and P. Bergonzo, Diamond Relat. Mater. **17**, 1235 (2008).
[22] I. Stenger, M.-A. Pinault-Thaury, T. Kociniewski, A. Lusson, E. Chikoidze, F. Jomard, Y. Dumont, J. Chevallier, and J. Barjon, J. Appl. Phys. **114**, 073711 (2013).
[23] H. Kato, H. Umezawa, N. Tokuda, D. Takeuchi, H. Okushi, and S. Yamasaki, Appl. Phys. Lett. **93**, 202103 (2008).
[24] R. Jones, J. E. Lowther, and J. Goss, Appl. Phys. Lett. **69**, 2489 (1996).
[25] S. Dannefaer, W. Zhu, T. Bretagnon, and D. Kerr, Phys. Rev. B **53**, 1979 (1996).
[26] V. Nadolinny, A. Komarovskikh, Y. Pal'yanov, and I. Kupriyanov, Phys. Status Solidi A **210**, 2078 (2013).
[27] V. Nadolinny, A. Komarovskikh, and Y. Palyanov, Crystals **7**, 237 (2017).
[28] C. Glover, M. E. Newton, P. M. Martineau, S. Quinn, and D. J. Twitchen, Phys. Rev. Lett. **92**, 135502 (2004).
[29] T. Miyazaki, H. Okushi, and T. Uda, Appl. Phys. Lett. **78**, 3977 (2001).
[30] C. Glover, M. E. Newton, P. Martineau, D. J. Twitchen, and J. M. Baker, Phys. Rev. Lett. **90**, 185507 (2003).
[31] J. P. Goss, R. Jones, M. I. Heggie, C. P. Ewels, P. R. Briddon, and S. Öberg, Phys. Rev. B **65**, 115207 (2002).

[32] L. G. Wang and A. Zunger, Phys. Rev. B **66**, 161202 (2002).
[33] T. Yamamoto, S. D. Janssens, R. Ohtani, D. Takeuchi, and S. Koizumi, Appl. Phys. Lett. **109**, 182102 (2016).
[34] J. P. Goss, P. R. Briddon, R. Jones, and S. Sque, J. Phys.: Condens. Matter **15**, S2903 (2003).
[35] T. Miyazaki, Phys. Status Solidi A **193**, 395 (2002).
[36] T. Nishimatsu, H. Katayama-Yoshida, and N. Orita, Physica B **302-303**, 149 (2001).
[37] J. Goss, P. Briddon, R. Jones, and S. Sque, Diamond Relat. Mater. **13**, 684 (2004).
[38] A. Kumar, J. Pernot, A. Deneuville, and L. Magaud, Phys. Rev. B **78**, 235114 (2008).
[39] P. E. Blöchl, Phys. Rev. B **50**, 17953 (1994).
[40] G. Kresse and J. Furthmüller, Phys. Rev. B **54**, 11169 (1996).
[41] J. Heyd, G. E. Scuseria, and M. Ernzerhof, J. Chem. Phys. **118**, 8207 (2003).
[42] J. Heyd, G. E. Scuseria, and M. Ernzerhof, J. Chem. Phys. **124**, 219906 (2006).
[43] S. Lany and A. Zunger, Phys. Rev. B **80**, 085202 (2009).
[44] K. Czelej, P. Śpiewak, and K. J. Kurzydłowski, Diamond Relat. Mater. **75**, 146 (2017).
[45] K. Czelej and P. Śpiewak, MRS Adv. **2**, 309 (2017).
[46] P. Śpiewak and K. J. Kurzydłowski, Phys. Rev. B **88**, 195204 (2013).
[47] H. J. Monkhorst and J. D. Pack, Phys. Rev. B **13**, 5188 (1976).
[48] G. Makov and M. C. Payne, Phys. Rev. B **51**, 4014 (1995).
[49] S. Lany and A. Zunger, Phys. Rev. B **78**, 235104 (2008).
[50] C. Freysoldt, J. Neugebauer, and C. G. Van de Walle, Phys. Rev. Lett. **102**, 016402 (2009).
[51] X. T. Trinh, K. Szász, T. Hornos, K. Kawahara, J. Suda, T. Kimoto, A. Gali, E. Janzén, and N. T. Son, Phys. Rev. B **88**, 235209 (2013).
[52] P. Deák, B. Aradi, T. Frauenheim, E. Janzén, and A. Gali, Phys. Rev. B **81**, 153203 (2010).
[53] A. Gali and J. R. Maze, Phys. Rev. B **88**, 235205 (2013).
[54] P. Deák, B. Aradi, M. Kaviani, T. Frauenheim, and A. Gali, Phys. Rev. B **89**, 075203 (2014).
[55] C. P. Herrero and R. Ramírez, Phys. Rev. Lett. **99**, 205504 (2007).
[56] C. Uzan-Saguy, C. Cytermann, B. Fizgeer, V. Richter, Y. Avigal, M. Shaanan, R. Brener, R. Kalish, E. Bustarret, and J. Chevallier, Diamond Relat. Mater. **11**, 316 (2002).
[57] A. Gali, E. Janzén, P. Deák, G. Kresse, and E. Kaxiras, Phys. Rev. Lett. **103**, 186404 (2009).
[58] G. Thiering and A. Gali, Phys. Rev. B **92**, 165203 (2015).
[59] M. J. Shaw, P. R. Briddon, J. P. Goss, M. J. Rayson, A. Kerridge, A. H. Harker, and A. M. Stoneham, Phys. Rev. Lett. **95**, 105502 (2005).
[60] U. F. S. D'Haenens-Johansson, A. M. Edmonds, M. E. Newton, J. P. Goss, P. R. Briddon, J. M. Baker, P. M. Martineau, R. U. A. Khan, D. J. Twitchen, and S. D. Williams, Phys. Rev. B **82**, 155205 (2010).
[61] G. Thiering and A. Gali, Phys. Rev. B **94**, 125202 (2016).
[62] T. Ivanova and B. Mavrin, Phys. Solid State **55**, 160 (2013).
[63] R. J. Nemanich and S. A. Solin, Phys. Rev. B **20**, 392 (1979).
[64] J. Zhang, C.-Z. Wang, Z. Z. Zhu, and V. V. Dobrovitski, Phys. Rev. B **84**, 035211 (2011).
[65] V. Ivády, T. Simon, J. R. Maze, I. A. Abrikosov, and A. Gali, Phys. Rev. B **90**, 235205 (2014).
[66] K. Szász, T. Hornos, M. Marsman, and A. Gali, Phys. Rev. B **88**, 075202 (2013).
[67] J. P. Goss, P. R. Briddon, M. J. Rayson, S. J. Sque, and R. Jones, Phys. Rev. B **72**, 035214 (2005).
[68] L. Childress, M. V. Gurudev Dutt, J. M. Taylor, A. S. Zibrov, F. Jelezko, J. Wrachtrup, P. R. Hemmer, and M. D. Lukin, Science **314**, 281 (2006).
[69] M. Eriksson, S. Coppersmith, and M. Lagally, MRS Bull. **38**, 794 (2013).
[70] W. F. Koehl, B. B. Buckley, F. J. Heremans, G. Calusine, and D. D. Awschalom, Nature (London) **479**, 84 (2011).
[71] G. W. Morley, P. Lueders, M. H. Mohammady, S. J. Balian, G. Aeppli, C. W. Kay, W. M. Witzel, G. Jeschke, and T. S. Monteiro, Nat. Mater. **12**, 103 (2013).
[72] G. D. Watkins and J. W. Corbett, Phys. Rev. **134**, A1359 (1964).
[73] S.-Y. Lee, M. Widmann, and T. Rendler, Nat. Nanotech. **8**, 487 (2013).